

Low finesse scattering and spectral drift of gravitational wave echoes

Han-Wen Hu^{1,2,*}, Cheng-Jun Fang^{1,2,†} and Zong-Kuan Guo^{1,2,3‡}

¹*Institute of Theoretical Physics, Chinese Academy of Sciences, P.O. Box 2735, Beijing 100190, China*

²*School of Physical Sciences, University of Chinese Academy of Sciences,*

No.19A Yuquan Road, Beijing 100049, China and

³*School of Fundamental Physics and Mathematical Sciences, Hangzhou Institute for Advanced Study,*

University of Chinese Academy of Sciences, Hangzhou 310024, China

Gravitational wave echoes serve as probes for quantum horizon corrections. While steady-state resonances are assumed in the search of gravitational wave echos, realistic barriers are expected to possess intrinsically low reflectivity. In this work, we investigate this low-finesse limit via time-domain simulations and demonstrate that early-time echoes behave as transient scattered wave packets rather than cavity eigenstates. A central finding is the identification of spectral drift, where the central frequency progressively redshifts. This evolution occurs because high-frequency components dissipate significantly faster than the fundamental mode due to the filtering effect of the potential barrier. To distinguish transient interference from genuine resonance, we establish a physical criterion based on cavity lifetime, identifying a critical reflectivity threshold of approximately 0.37. Since theoretical models typically operate deep within the overdamped regime below this limit, the resulting signals are spectrally non-stationary. We propose that detection strategies should shift towards dynamic time-frequency tracking to capture these drifting signatures.

I. INTRODUCTION

The detection of gravitational waves (GWs) by the LIGO-Virgo-KAGRA collaboration has confirmed the validity of general relativity in the strong-field regime and the Kerr geometry of remnant black holes (BHs) [1–3]. However, the classical description of the event horizon remains challenged by fundamental problems in quantum gravity, such as the information loss paradox [4]. Various quantum-corrected models, including fuzzballs [5], firewalls [6], and gravastars [7], as well as exotic compact objects (ECOs) like traversable wormholes [8–10], predict the existence of reflective boundaries or structure at the horizon scale [11]. A key observational signature of such near-horizon modifications is the emission of GW echoes: a train of post-merger pulses resulting from the trapping of radiation between the angular momentum barrier and the effective surface of the compact object [12–15].

The potential discovery of echoes would revolutionize fundamental physics, motivating extensive observational searches in LVK data. Early analyses employing phenomenological templates claimed tentative evidence for echoes in O1/O2 events [16], though these results remain controversial due to the statistical significance of noise artifacts [17, 18]. Subsequent searches have diversified into two main paradigms. The first one is template-based methods, which construct waveforms by summing geometric series of reflections [19, 20] or phenomenological fitting of numerical solutions [21], often assuming a steady-state comb structure in the frequency domain [22, 23]. The second one is called morphology-independent searches [24, 25], such as those based on the Coherent WaveBurst (cWB) algorithm, which impose minimal assumptions on the signal shape [24]. Despite these efforts, no statistically significant evidence

for echoes has been claimed in the latest O3 catalogs [2, 26, 27], raising the question of whether current search templates are physically faithful to the signal dynamics in realistic astrophysical environments.

A critical, yet often overlooked, factor governing echo phenomenology is the finesse of the effective cavity. Theoretical developments suggest that realistic ECO boundaries may interact non-trivially with the trapped radiation. While potential barriers are known to act as high-pass filters [28–31], we find that in the low-finesse limit, this filtering does not lead to stationary modes but instead drives a continuous spectral drift, where the signal’s central frequency progressively redshifts. Furthermore, mechanisms such as Boltzmann reflectivity [32, 33], spectral instability [34], or energy redistribution in complex topologies (e.g., wormholes) [35] imply that the system may operate in a low-reflectivity regime [36]. In this limit, the characteristic timescale for resonance formation exceeds the dissipation timescale, preventing the establishment of the stationary quasi-normal modes (QNMs) assumed by comb-based searches.

In this work, we elucidate the physical nature of early-time echoes in the realistic low-finesse limit. By combining time-domain numerical simulations with a transfer-matrix analysis, we demonstrate that early echoes are intrinsically transient scattered wave packets rather than steady-state cavity eigenmodes. Crucially, we identify a ubiquitous phenomenon of spectral drift: due to the high-frequency filtering of the potential barrier, the central frequency of the echo train progressively redshifts over time. This dynamic evolution fundamentally violates the frequency-locking assumption inherent in static comb templates and aligns with the null results of standard searches. Our findings advocate for a paradigm shift towards dynamic time-frequency tracking or unmodeled

burst strategies to capture these elusive spectral fingerprints.

II. THE FIRST ECHO MODULATED BY REFLECTIVITY

To elucidate the physical nature of early-time GW echoes, we formulate the time-domain evolution of the perturbed BH as a one-dimensional quantum mechanical scattering problem. Consider axial gravitational perturbations on a Schwarzschild BH background. In the frequency domain, the radial master variable $\Psi(r_*, \omega)$ satisfies the Regge-Wheeler equation

$$\frac{d^2\Psi(r_*, \omega)}{dr_*^2} + [\omega^2 - V_{\text{eff}}(r_*)] \Psi(r_*, \omega) = 0, \quad (1)$$

where r_* denotes the tortoise coordinate. The effective potential $V_{\text{eff}}(r_*)$ comprises the standard Regge-Wheeler potential barrier near the photon sphere and a perturbative potential bump located at a macroscopic distance L .

A. Transfer Matrix theory

We adopt the transfer matrix method to connect the wave functions across different scattering regions[37–39]. We define a state vector $\Phi(r_*)$ representing the amplitudes of the outgoing and ingoing waves

$$\Phi(r_*) = \begin{pmatrix} A(r_*) \\ B(r_*) \end{pmatrix}, \quad (2)$$

corresponding to $\Psi(r_*) \sim A(r_*)e^{i\omega r_*} + B(r_*)e^{-i\omega r_*}$. The global scattering properties are encoded in the global transfer matrix $\mathbf{M}(\omega)$, which relates the state at the horizon Φ_H to the state at spatial infinity Φ_{inf}

$$\Phi_{\text{inf}} = \mathbf{M}(\omega) \cdot \Phi_H = (\mathbf{T}_{\text{bump}} \cdot \mathbf{P}_L \cdot \mathbf{T}_{\text{RW}}) \cdot \Phi_H, \quad (3)$$

where \mathbf{T} represents the local transfer matrix for each barrier, and $\mathbf{P}_L = \text{diag}(e^{i\omega L}, e^{-i\omega L})$ accounts for the geometric phase accumulation over the cavity length L .

By imposing the physical boundary condition of no incoming radiation from infinity and considering an initial source excitation $S_{\text{in}}(\omega)$ propagating inward from the cavity, we derive the observed waveform $\tilde{\Psi}_{\text{obs}}$ at infinity. The global transfer function is obtained by solving the matrix equation for the transmitted amplitude

$$\tilde{\Psi}_{\text{obs}}(\omega) = \frac{T_{\text{bump}}(\omega)R_{\text{RW}}(\omega)e^{i\omega L}}{1 - R_{\text{RW}}(\omega)R_{\text{bump}}(\omega)e^{2i\omega L}} S_{\text{in}}(\omega). \quad (4)$$

The complex poles of this transfer function, defined by the condition $1 - \mathcal{L}(\omega_n) = 0$, where $\mathcal{L}(\omega)$ is the loop propagator, correspond to the quasinormal modes (QNMs)

of the system. These poles describe the steady-state resonance formed after infinite reflections. However, for early-time observations constrained by causality, the steady-state resonance has not yet been established. In the regime of low reflectivity ($|R_{\text{bump}}| \ll 1$), the appropriate physical description is provided by the geometric series expansion of the transfer function

$$\tilde{\Psi}_{\text{obs}}(\omega) \equiv \tilde{\Psi}_{\text{prompt}}(\omega) \sum_{n=0}^{\infty} [R_{\text{RW}}(\omega)R_{\text{bump}}(\omega)e^{2i\omega L}]^n, \quad (5)$$

where the $n = 1$ term corresponds to the first echo. Its explicit form,

$$\tilde{\Psi}_{\text{echo}}^{(1)} = \tilde{\Psi}_{\text{prompt}} \cdot \mathcal{L}(\omega), \quad (6)$$

reveals that the first echo is not an independent excitation of cavity eigenmodes, but rather the prompt wave packet modulated by the loop propagator $\mathcal{L}(\omega)$. This modulation effect is completely determined by the complex reflection coefficients of the two scattering barriers and the geometric phase. Therefore, in the transient limit of low reflectivity, the physical essence of the echo signal is the superposition of scattered wave packets rather than the resonant excitation of QNM poles.

To validate the absence of a comb spectrum under low reflectivity, we performed time-domain numerical simulations of the Regge-Wheeler equation. We employed a Pöschl-Teller potential barrier $V_{\text{bump}}(r_*) = \epsilon \text{sech}^2(r_* - L)$ as the perturbation model, setting the perturbation amplitude to $\epsilon = 10^{-5}$. This parameter choice aims to simulate realistic astrophysical scenarios, such as quantum horizon corrections or extremely diffuse dark matter halos, where the intrinsic reflectivity of the external barrier is extremely low, placing the system strictly in the low-finesse regime¹. We set the cavity length to $L = 180$. This geometric parameter is crucial for physical analysis as it ensures a clear dynamical separation between the prompt ringdown signal and the subsequent echo signals in the time domain. Specifically, when the first echo arrives at $t \simeq 2L$, the prompt ringdown of the BH has already decayed to the power-law tail stage governed by the multipole moments. At this stage, the prompt amplitude is sufficiently low to prevent time-domain interference between the echo wave packet and the strong QNM ringing, thereby providing a clean background for spectral analysis.

¹ Physically, such horizon-scale modifications, whether arising from quantum corrections or effective fluids, are constrained by current observational consistencies with GR to remain strictly perturbative. Consequently, the amplitude of the potential bump is inherently microscopic, enforcing a low-reflectivity regime ($|R_{\text{bump}}| \ll 1$) where the effective cavity is intrinsically overdamped.

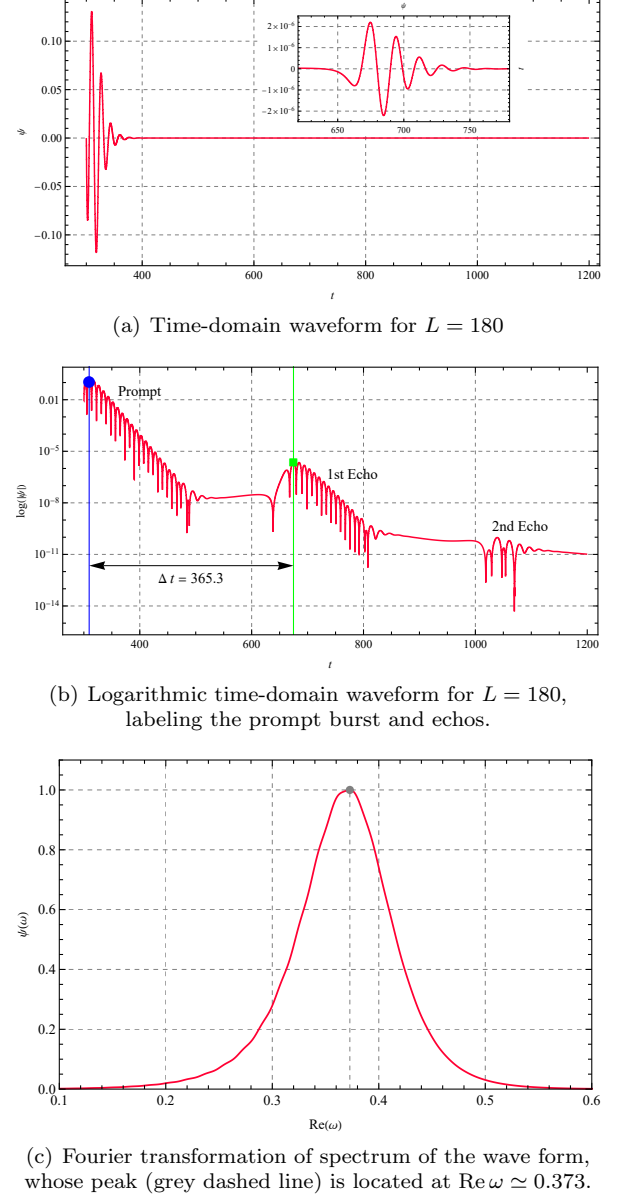
Fig. 1(a) and 1(b) displays the time-domain waveform obtained from the numerical simulation. The first echo appears as an isolated wave packet at $t \simeq 2L$, residing atop the flat power-law tail. This indicates that the echo has decoupled from the initial ringing of the BH, behaving as an independent scattering event. Although a second echo appears at a later time in the simulation, its waveform exhibits significant distortion due to dispersive effects accumulated over multiple reflections; therefore, our quantitative analysis focuses on the first echo, which possesses the highest signal to noise ratio and the clearest physical features. To explore the frequency-domain characteristics of the waveform, we computed its Fourier transform, with the results shown in Fig. 1(c). The spectrum presents a smooth, single-peak profile nearly centered on the Schwarzschild fundamental frequency. The energy distribution passes smoothly through the theoretical QNM comb frequencies predicted by the steady-state pole condition $1 - \mathcal{L}(\omega_n) = 0$, without any sign of resonant enhancement or discretization. To physically interpret this no-comb spectrum phenomenon, we performed a semi-quantitative scattering analysis combining the numerical simulation parameters. The frequency-domain form of the first echo is given by Eq. (6), where the magnitude of the loop propagator \mathcal{L} is determined by the reflection coefficients of the two barriers. Using the numerical integration, we precisely calculated the intrinsic reflectivity at the Schwarzschild fundamental frequency $\omega_0 \simeq 0.3737 - 0.0889i$, yielding a reflection coefficient of

$$|R_{\text{RW}}| \simeq 0.729, \quad |R_{\text{bump}}| \simeq 2.15 \times 10^{-5} \quad (7)$$

for the Regge-Wheeler barrier and perturbative bump, respectively. From this, the loop gain for a single round trip can be estimated as $|\mathcal{L}(\omega_0)| = |R_{\text{RW}}R_{\text{bump}}| \simeq 1.57 \times 10^{-5}$. This extremely small loop gain implies that the system is in a deeply overdamped state. The energy within the cavity is almost completely dissipated during a single round trip, making it impossible to establish sharp resonance peaks observable on the real axis through multiple coherent superpositions. Therefore, the smooth spectrum observed in Fig. 1(c) confirms that in this transient process, the geometric series has not yet summed to form poles, and the so-called comb spectrum does not physically exist. What we observe is merely a broadband scattering wave packet modulated by weak scattering phases.

B. Numerical Analysis

To distinguish whether the first echo represents a trapped cavity eigenmode or a transient scattering wave packet, we contrast the steady-state theoretical prediction with numerical observations. If the system were to reach a steady state, the spectral content would be quantized by the pole condition of the global transfer



(c) Fourier transformation of spectrum of the wave form, whose peak (grey dashed line) is located at $\text{Re}\omega \simeq 0.373$.

FIG. 1: Time-domain waveform and its Fourier transform

function, $1 - R_{\text{RW}}(\omega)R_{\text{bump}}(\omega)e^{2i\omega L} = 0$. Expressing the complex reflection coefficients as $R_j(\omega) = |R_j|e^{i\delta_j(\omega)}$ (where $j \in \{\text{RW}, \text{bump}\}$), the phase condition for the poles requires

$$2\omega_n L + \delta_{\text{tot}}(\omega_n) = 2\pi n, \quad (n \in \mathbb{Z}), \quad (8)$$

where $\delta_{\text{tot}} = \delta_{\text{RW}} + \delta_{\text{bump}}$ is the total intrinsic phase shift per round trip. To derive the frequency shift implied by this condition, we perform a perturbation analysis around the geometric cavity frequency $\omega_n^{(0)} = n\pi/L$. We assume the resonant frequency is $\omega_n = \omega_n^{(0)} + \Delta\omega_n$, with $\Delta\omega_n \ll \omega_n^{(0)}$, we substitute this into the phase constraint. Using the identity $2\omega_n^{(0)} L = 2\pi n$, the leading geometric

term cancels out. This cancellation isolates the frequency shift, yielding the analytical prediction for the steady-state regime

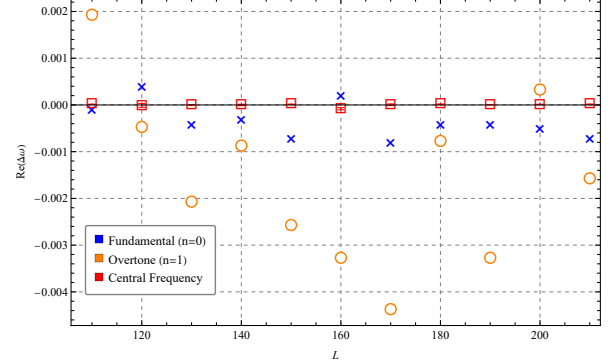
$$\Delta\omega_n \simeq -\frac{\delta_{\text{tot}}(\omega_n)}{2L}. \quad (9)$$

We calculated the theoretical parameters at the Schwarzschild fundamental frequency $\omega_0 \simeq 0.374$ using the numerical integration, finding $\delta_{\text{RW}} \simeq -1.07$ rad and $\delta_{\text{bump}} \simeq -1.57$ rad. The total phase $\delta_{\text{tot}} \simeq -2.64$ rad is negative, which implies that a steady-state mode should exhibit a distinct blue shift scaling with $1/L$.

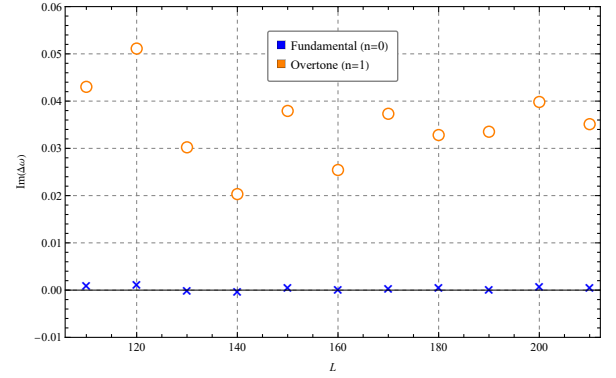
However, numerical observations of the first echo refute this steady-state prediction. Fig. 2(a) presents the real part of the frequency shift for the effective central frequency, extracted via the MPM (see App. A for a rigorous convergence test verifying the numerical stability of these spectral features). Contrary to the predicted $1/L$ blue shift, the central frequency (red squares) remains strictly locked to the baseline $\Delta\omega_c \simeq 0$. This confirms that the first echo is governed by the geometric series expansion ($\Psi^{(1)} \sim |R_{\text{RW}}R_{\text{bump}}|e^{i\delta_{\text{tot}}}\Psi_{\text{prompt}}$) rather than the pole summation. The phase term $e^{i\delta_{\text{tot}}}$ acts as a modulation factor in the numerator, not a quantization constraint. Consequently, the non-zero phase δ_{tot} converts into a Wigner time delay via $\tau \simeq \partial\delta_{\text{tot}}/\partial\omega$ [40], enforcing causality, i.e. $\Delta t > 2L$, without shifting the spectral central frequency. Microscopic analysis further highlights the transient nature of the signal. Fig. 2(b) displays the imaginary frequency shifts for the fundamental mode and the first overtone. While the macroscopic central frequency remains stable, the individually extracted components exhibit significant numerical fluctuations. The overtone (orange circles), in particular, shows fluctuations across different cavity lengths L , indicating that the extraction of this rapidly decaying mode is sensitive to the geometric phase. However, it maintains a recognizable trajectory, indicating that while the overtone is physically present in the first echo, it represents a more transient and rapidly decaying component of the wave packet compared to the dominant fundamental mode. The rapid decay of this overtone component acts as the seed for the macroscopic spectral drift that dominates subsequent echoes. Thus, while microscopic components fluctuate due to the lack of a steady state, their coherent superposition ensures the transport stability of the macroscopic wave packet.

III. SPECTRAL DRIFT IN THE TEMPORAL EVOLUTION

Having established that the first echo is a transient wave packet rather than a cavity eigenmode, we now extend our inquiry to the temporal evolution of the subsequent signal train. This multi-echo regime serves as a



(a) The real part of the frequency shift $\text{Re}(\Delta\omega)$. The central frequency remains locked to the baseline ($\Delta\omega \simeq 0$) independent of L , defying the $1/L$ blue shift predicted by the steady-state resonance condition.



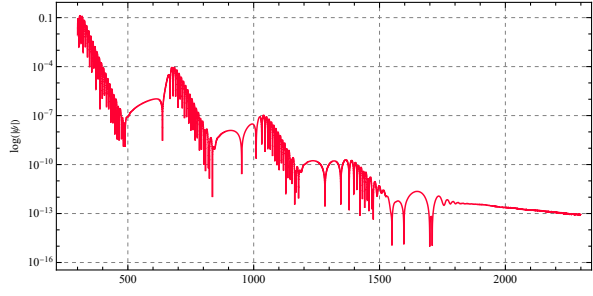
(b) The imaginary part of the frequency shift $\text{Im}(\Delta\omega)$. While the fundamental mode (blue crosses) remains stable and the first overtone (orange circles) exhibits larger fluctuations than the fundamental but remains spectrally resolvable. This indicates that while highly damped harmonics are less stable, they are still transiently excited before rapid dissipation.

FIG. 2: Spectral stability analysis of the first GW echo as a function of cavity length $L \in [110, 210]$. The frequency shifts $\Delta\omega$ are measured relative to the fundamental Schwarzschild QNM. The effective central frequency (red squares) is defined as the amplitude-weighted mean of the real parts of the eigenfrequencies extracted via MPM, $\omega_c = \sum_j |A_j| \text{Re}(\omega_j) / \sum_j |A_j|$, where A_j and ω_j are the amplitude and complex frequency of the j -th component.

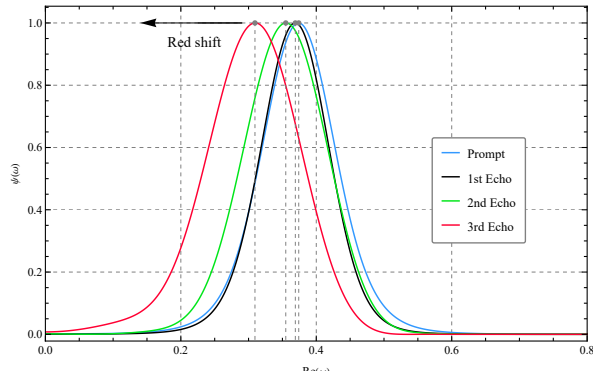
critical discriminator between the steady-state resonance paradigm and the transient scattering framework. If the system were to lock into a steady state, as posited by the comb model, successive echoes would be forced to ring at fixed quantization frequencies ω_n , exhibiting strict time-translation invariance. In contrast, the scattering perspective predicts a dynamic spectral evolution governed by the iterative modulation of the frequency-dependent transfer function. To rigorously test this, we examine the

spectral content of the secondary and tertiary echoes. For this specific analysis, we employ another model with an enhanced perturbation amplitude of $\epsilon = 4 \times 10^{-4}$, distinct from the astrophysical value. This parameter choice improves the signal-to-noise ratio of late-time echoes, allowing us to resolve their spectral features clearly without qualitative loss of the underlying physical mechanism.

Theoretically, the evolution is driven by the reflectivity of the Regge-Wheeler potential, $|R_{RW}(\omega)|$. In the frequency range of interest, the potential barrier is more transparent to high-frequency modes—which readily transmit into the horizon—and more reflective to low-frequency modes. Consequently, the barrier acts as an effective low-pass filter. With each round trip, the wave packet is multiplied by the reflectivity profile, causing a cumulative suppression of high-frequency components and a systematic redshift of the effective central frequency. To visualize this evolutionary process, Fig. 3 presents the evolution of the first three echoes in both time and frequency domains.



(a) Time-domain waveform $\Psi(t)$. The signal exhibits a clear sequence of echoes with dispersive broadening.



(b) Superimposed spectral profiles of the prompt signal and the first three echoes. The spectra are computed by isolating the linear ringdown phase of each echo packet from the logarithmic waveform. A significant spectral drift is observed: the central frequency redshifts progressively from the prompt value (blue) to the 3rd echo (red).

FIG. 3: Temporal and spectral evolution of the first three echoes in the enhanced perturbation model, $\epsilon = 4 \times 10^{-4}$.

Specifically, to ensure spectral accuracy, we extract

each echo segment by isolating the linear decay phase (ringdown) of the wave packet from the logarithmic waveform, avoiding the contamination from the non-dispersive prompt reflection edge. The numerical result reveals a striking spectral trajectory that fundamentally violates the frequency-locking prediction. In the time domain waveform Fig. 3(a), the wave packets exhibit progressive dispersive broadening. The corresponding spectral analysis Fig. 3(b) quantifies this drift. The first echo (black curve) retains the spectral characteristics of the prompt ringdown (blue curve), centered near the Schwarzschild fundamental frequency. However, as the signal undergoes repeated filtering, a dramatic spectral drift emerges. The central frequency shifts visibly to the left in the second echo (green curve) and continues to redshift in the third echo (red curve). This progressive redshift confirms that the echoes are not eigenmodes oscillating at a fixed tone, but rather transient wave packets “sliding” down the frequency spectrum as they are eroded by the horizon’s filtering effect. This finding renders static matched-filter templates (based on fixed combs) physically inadequate for early-time detection, necessitating a paradigm shift towards tracking drifting effective central frequencies.

This progressive redshift ($\Delta\omega/\omega_0 \sim 25\%$ by the 3rd Echo) elucidates the physical origin of the cavity modes. The “static comb modes” are mathematically the result of the infinite interference of these drifting packets. However, our observation confirms that in the realistic low-reflectivity regime, the system is overdamped. The high-frequency components are eroded by the horizon before they can constructively interfere to form stable, high-Q eigenstates. Thus, the signal remains in the transient phase, characterized by a drifting Schwarzschild wave packet rather than a locked cavity resonance. This implies that for astrophysical BHs, the echo is not a single spectral entity but a dynamical process where the frequency slides over time. Furthermore, due to the low reflectivity, the echo amplitude decays rapidly until it is inevitably submerged by the power-law tail [30].

IV. FROM SCATTERING TO RESONANCE

The spectral drift observed in the individual echoes presents a striking contrast when compared with the global Fourier transform of the full time-domain waveform (prompt signal plus 3 echoes), which displays a distinct periodic “sawtooth” modulation as shown in Fig. 4. To rigorously distinguish whether these features represent genuine QNMs or merely transient interference fringes, we formulate a spectral theory based on finite multi-beam interference. We model the frequency-domain signal as the coherent superposition of the prompt wave packet $\tilde{\Psi}_{\text{prompt}}$ and N subsequent echoes. Let R denote the observed amplitude ratio between successive echoes, which empirically quantifies the loop re-

flectivity factor $R \equiv |R_{\text{RW}}R_{\text{bump}}|$. Consistent with Eq. (5), the observed spectrum is strictly described by the partial sum of the geometric series

$$\tilde{\Psi}_N(\omega) = \tilde{\Psi}_{\text{prompt}}(\omega) \frac{1 - (Re^{2i\omega L})^{N+1}}{1 - Re^{2i\omega L}}. \quad (10)$$

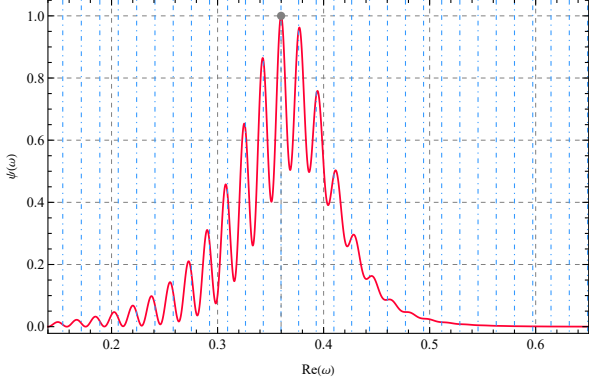


FIG. 4: Global Fourier spectrum of the full time-domain waveform for the enhanced perturbation model with amplitude $\epsilon = 4 \times 10^{-4}$ and cavity length $L = 180$. The spectrum (red solid line) exhibits a distinct periodic ‘sawtooth’ modulation. The vertical blue dashed lines indicate the theoretical cavity eigenfrequencies calculated via the shooting method, nearly demonstrating a precise alignment with the numerical peaks. The grey dot marks the dominant spectral peak located at $\text{Re}(\omega) \simeq 0.35989$.

The physical nature of the spectrum is strictly governed by the magnitude of R . We first analyze the scattering limit characteristic of realistic astrophysical environments, where the observed amplitude ratio is extremely low ($R \sim 10^{-5}$, see Fig. 1(b)). Consequently, truncated to $N = 1$, the power spectrum degenerates into a simple cosine modulation

$$|\tilde{\Psi}_N(\omega)|^2 \simeq |\tilde{\Psi}_{\text{prompt}}|^2 [1 + 2R \cos(2\omega L)]. \quad (11)$$

This expression describes the broad sinusoidal sawtooth pattern observed in Fig. 4. However, to rigorously determine whether such a feature constitutes a resonance mode, we must examine the exact spectral line shape without truncation. In the low reflectivity regime, the higher-order term in the numerator vanishes rapidly, i.e., $R^{N+1} \simeq 0$, even for small N . Thus, the spectrum is fundamentally governed by the denominator of the transfer function, following the general Airy distribution

$$|\tilde{\Psi}_N(\omega)|^2 \simeq \frac{|\tilde{\Psi}_{\text{prompt}}|^2}{(1 - R)^2 + 4R \sin^2(\omega L)}. \quad (12)$$

To physically identify a spectral feature as a resonance mode, it must first satisfy a fundamental existence condition, the peak must be distinguishable from the background continuum by possessing a definable Full Width

at Half Maximum (FWHM). A physically resolvable resonance peak exists if and only if the spectral minimum drops below half of the spectral maximum, $I_{\min} \leq I_{\max}/2$. Substituting the extrema of the Airy function into this inequality imposes a fundamental lower bound on the reflectivity

$$\frac{1}{(1 + R)^2} \leq \frac{1}{2(1 - R)^2}, \quad (13)$$

which means $R \geq 0.17$. If this condition is met, a further resolvability condition is required to define the feature as a high-Q mode: the linewidth must be significantly narrower than the free spectral range $\Delta\omega_{\text{FSR}} = \pi/L$ to ensure sharp mode separation. While $\mathcal{F} \gtrsim 1$ allows for barely resolvable peaks, a genuine resonance requires the wave packet to survive at least one round trip, which imposes a stricter threshold $R \gtrsim e^{-1}$. As derived in App. B, this time-domain causality condition ($\tau \gtrsim 2L$) is physically equivalent to the frequency-domain requirement that the finesse exceeds π ($\mathcal{F} \gtrsim \pi$), i.e.,

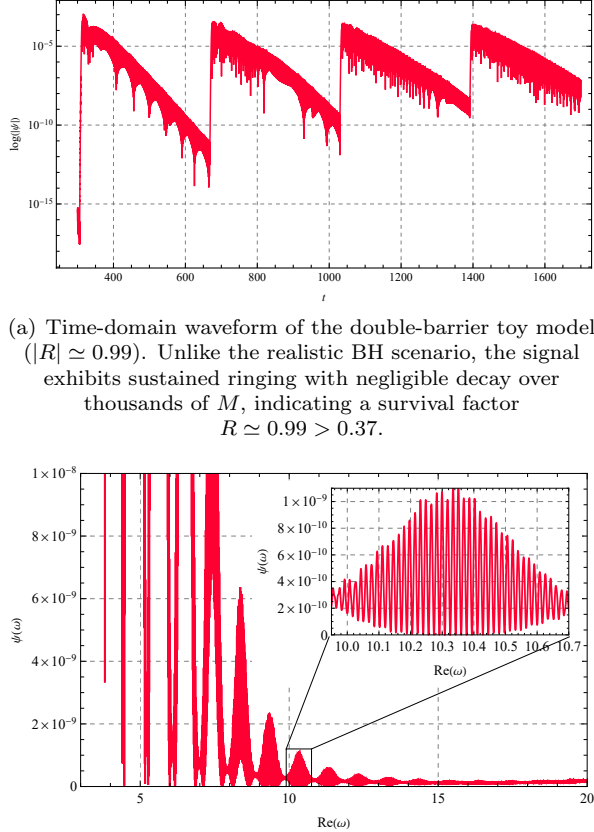
$$\frac{\pi\sqrt{R}}{1 - R} \gtrsim \pi, \quad (14)$$

which yields the critical reflectivity $R \gtrsim 0.38$, numerically consistent with the lifetime bound $R \gtrsim e^{-1} \simeq 0.37$. This threshold elucidates the convergence issues reported in Ref. [30], where the reflectivity ($R \simeq 0.17$ for $\epsilon = 0.1$) falls below the stability limit. In this overdamped regime, static QNM templates are physically ill-defined as the signal is a continuously drifting wave packet.

We apply these criteria to quantitatively evaluate two representative models. First, for the realistic BH perturbation $R \ll 1$, even the fundamental existence criterion is violated, $10^{-3} \ll 0.17$. Mathematically, the equation for FWHM has no real solution. The peaks observed in Fig. 4 are broad sinusoidal modulations that never decay to half-power, characteristic of low-finesse interference fringes, analogous to Young’s double-slit interference. The periodic structure is thus an artifact of the finite superposition of the prompt signal and the first weak echo.

In contrast, for the waveform of double-barrier toy model shown in the Fig. 5(a), the high reflectivity ($R \simeq 0.99$) satisfies both the existence and resolvability criteria Eq. (14). Consequently, its spectrum, as shown in Fig. 5(b), exhibits sharp Lorentzian combs with well-defined FWHM, confirming the formation of genuine QNMs.

In summary, we conclude that the comb-like features in the first three echoes are spectral artifacts of low-finesse interference. Since the empirical survival factor $R \sim 10^{-6}$ is orders of magnitude below the resonance thresholds, the system physically operates as a single-scattering interferometer, not a resonator.



(a) Time-domain waveform of the double-barrier toy model ($|R| \simeq 0.99$). Unlike the realistic BH scenario, the signal exhibits sustained ringing with negligible decay over thousands of M , indicating a survival factor $R \simeq 0.99 > 0.37$.

(b) Global Fourier spectrum of the waveform in panel (a). The spectrum displays extremely sharp, well-separated peaks. The inset highlights the fine structure of the Lorentzian combs, which possess a well-defined FWHM much narrower than the spectral spacing. This confirms that when the reflectivity criterion is met, the scattering process transitions into stable cavity eigenmodes.

FIG. 5: The hallmark of genuine resonance in the high-finesse regime. Here we take cavity length $L = 180$, barrier height $V = 10$, and width $w = 3$.

V. CONCLUSION AND DISCUSSION

In this work, we elucidated the physical nature of early-time GW echoes. Our central finding is that in the low-finesse limit, echoes are intrinsically transient scattered wave packets rather than steady-state cavity modes. The observed comb features are merely interference fringes—analogous to Young’s double-slit experiment—rather than high-Q resonances. Crucially, due to the high-frequency filtering of the horizon barrier, the echo packet undergoes significant spectral drift, systematically redshifting over time. This dynamic behavior contrasts sharply with the frequency-locking predicted by standard resonance models.

These findings offer fresh insights into ECOs characterized by imperfect boundaries. As demonstrated in Ref. [28], the potential barrier acts as a spin and frequency dependent high-pass filter, which naturally modulates the

spectrum and decreases the frequency content of subsequent echoes. Our work quantifies this mechanism in the low-reflectivity regime ($R \ll 1$), showing that the system is overdamped; high-frequency components dissipate much faster than the fundamental, preventing the formation of long-lived, high-Q resonances. This aligns with the broader theoretical arguments in Ref. [35], which suggest that the redistribution of energy (e.g., in wormhole models) can render echoes extremely weak and unobservable. Our proposed finesse criterion provides the physical threshold to distinguish these transient scattering artifacts from genuine long-lived modes.

The phenomenon of spectral drift carries profound implications for data analysis. Current search strategies, such as the uniform comb analysis developed in Ref. [23], are premised on the assumption that the signal consists of steady-state harmonics with fixed quantization frequencies. However, our results indicate that early echoes exhibit dynamic redshift rather than static quantization. Matching a drifting signal with a static template inevitably induces severe phase mismatches. This physical mismatch may explain the absence of statistically significant comb signatures in events like GW150914.

Consequently, we suggest shifting the search paradigm from static template matching to dynamic time-frequency tracking. A robust alternative lies in unmodeled transient search pipelines, such as the Coherent WaveBurst method employed in Ref. [24]. By imposing minimal assumptions on the waveform morphology, such methods are better suited to capture sliding wave packets that drift in frequency. Future work will extend this framework to Kerr spacetimes, investigating whether superradiant instabilities can overcome low-finesse damping to eventually induce genuine resonances at late times.

ACKNOWLEDGMENTS

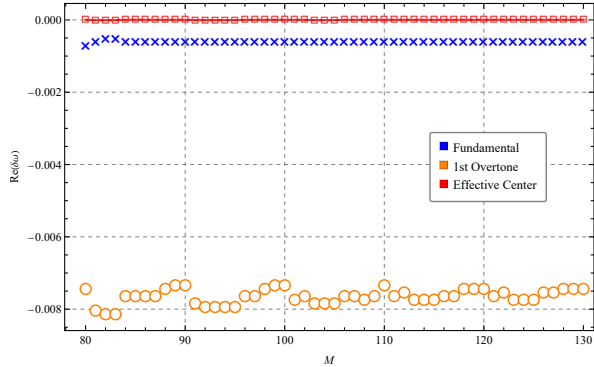
H.-W.Hu is grateful for C.Lan for useful discussions. This work is supported in part by the National Key Research and Development Program of China No. 2020YFC2201501, in part by the National Natural Science Foundation of China No. 12475067 and No. 12235019.

Appendix A: Numerical stability and convergence of spectral extraction

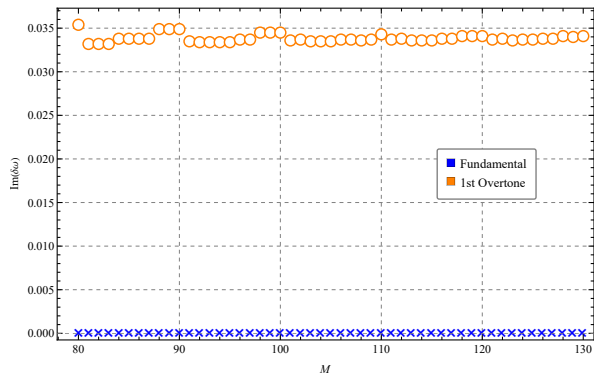
To ensure that the spectral features identified in the main text are intrinsic physical observables rather than numerical artifacts, we performed a rigorous convergence test with respect to the MPM order parameter M . The analysis focuses on the first echo waveform for a representative cavity length $L = 180$. Consistent with the main

text, the data segment was selected by isolating the linear decay phase of ringdown in the logarithmic waveform Fig. 1(b).

We scanned M over the range [80, 130]. To clearly visualize the accuracy and physical shifts, Fig. 6 plots the frequency deviations $\delta\omega$ relative to the standard Schwarzschild QNMs. For the fundamental and first overtone, the deviations are defined as $\delta\omega = \omega_{\text{extracted}} - \omega_{\text{Schw}}^{(n)}$, using the theoretical values $\omega_{\text{Schw}}^{(0)} \simeq 0.3737 - 0.0889i$ and $\omega_{\text{Schw}}^{(1)} \simeq 0.3468 - 0.2739i$. For the effective central frequency, we plot the deviation from its mean value across the scan.



(a) The deviation of the real part of the frequencies, $\text{Re}(\delta\omega)$. The fundamental mode (blue) matches the Schwarzschild prediction almost perfectly. The overtone (orange) exhibits a stable negative shift relative to the vacuum theory, confirming it is a physical mode perturbed by the barrier rather than a numerical artifact.



(b) The deviation of the imaginary part, $\text{Im}(\delta\omega)$. The stability of the overtone's deviation confirms its physical presence despite its rapid decay.

FIG. 6: Convergence test of spectral deviations with respect to the MPM order $M \in [80, 130]$ for the first echo at $L = 180$.

For real part deviations, as shown in Fig. 6(a), the real frequency deviation of the fundamental mode (blue crosses) is negligible ($\sim 10^{-4}$), confirming that the dominant oscillation is precisely locked to the Schwarzschild geometry. The effective central frequency (red squares) also exhibits excellent stability. Crucially, the first over-

tone (orange circles) shows a stable, non-zero deviation of $\text{Re}(\delta\omega) \sim -0.008$. This indicates that the overtone is physically present and numerically stable; however, its frequency is slightly redshifted compared to the vacuum value, likely due to the modification of the effective potential by the external barrier. As shown in Fig. 6(b), the imaginary deviation of the fundamental mode is consistently near zero. The overtone shows a positive deviation of $\text{Im}(\delta\omega) \simeq 0.035$, implying a measured decay rate of $\text{Im}(\omega) \sim -0.24$. Although this differs from the vacuum value, the stability of this deviation across the range of M confirms that the overtone is a distinct, physical component of the wave packet with a well-defined decay rate, rather than a random noise pole.

Appendix B: Equivalence between cavity lifetime and finesse

Consider a wave packet bouncing between two barriers separated by a distance L . The round-trip time is given by $T = 2L$. Let $R \equiv |R_{\text{RW}}R_{\text{bump}}|$ denote the combined amplitude reflectivity per round trip. In the geometric optics limit, the amplitude of the wave packet after n round trips decays as $|\Psi_n| \propto R^n$. Expressing this as a continuous function of time $t = n \cdot 2L$, the decay law is

$$|\Psi(t)| \propto R^{\frac{t}{2L}} = \exp\left(\frac{t}{2L} \log R\right) \equiv \exp\left(-\frac{t}{\tau}\right), \quad (\text{B1})$$

where τ is the characteristic photon lifetime of the cavity. Comparing the exponents yields

$$\tau = \frac{2L}{|\log R|}. \quad (\text{B2})$$

For a physical resonance to form, the stored energy must survive long enough to complete at least one closed loop to establish a coherent standing wave pattern. This imposes the causality condition $\tau \gtrsim 2L$. Substituting Eq. (B2) into this inequality yields

$$R \gtrsim e^{-1} \simeq 0.368. \quad (\text{B3})$$

In the frequency domain, the resolvability of spectral modes is characterized by the finesse \mathcal{F} , defined as the ratio of the free spectral range $\Delta\omega_{\text{FSR}} = \pi/L$ to the full width at half maximum $\delta\omega$

$$\mathcal{F} \equiv \frac{\Delta\omega_{\text{FSR}}}{\delta\omega} = \frac{\pi\sqrt{R}}{1-R}. \quad (\text{B4})$$

We now test the value of the finesse at the critical reflectivity threshold derived from the time-domain argument. Substituting $R = e^{-1}$ into Eq. (B4),

$$\mathcal{F}_{\text{crit}} \simeq 0.959\pi \simeq 3.01. \quad (\text{B5})$$

This result reveals a fundamental physical duality: the causality requirement for the wave packet to survive one

round trip is mathematically nearly equivalent to the standard optical criterion for high-finesse cavities $\mathcal{F} \simeq \pi$. Therefore, the threshold $\mathcal{F} \gtrsim \pi$ is not an arbitrary choice but a direct consequence of the transition from a transient, overdamped scattering regime $\tau < T$ to a resonant, underdamped regime $\tau > T$.

* huhanwen@itp.ac.cn

† fangchengjun@itp.ac.cn

‡ guozk@itp.ac.cn

[1] B. P. Abbott *et al.* (LIGO Scientific, Virgo), Phys. Rev. Lett. **116**, 221101 (2016), [Erratum: Phys. Rev. Lett. 121, 129902 (2018)], arXiv:1602.03841 [gr-qc].

[2] R. Abbott *et al.* (LIGO Scientific, VIRGO, KAGRA), Phys. Rev. D **112**, 084080 (2025), arXiv:2112.06861 [gr-qc].

[3] R. Abbott *et al.* (KAGRA, VIRGO, LIGO Scientific), Phys. Rev. X **13**, 041039 (2023), arXiv:2111.03606 [gr-qc].

[4] S. D. Mathur, Class. Quant. Grav. **26**, 224001 (2009), arXiv:0909.1038 [hep-th].

[5] S. D. Mathur, Fortsch. Phys. **53**, 793 (2005), arXiv:hep-th/0502050.

[6] A. Almheiri, D. Marolf, J. Polchinski, and J. Sully, JHEP **02**, 062 (2013), arXiv:1207.3123 [hep-th].

[7] P. O. Mazur and E. Mottola, Universe **9**, 88 (2023), arXiv:gr-qc/0109035.

[8] T. Damour and S. N. Solodukhin, Phys. Rev. D **76**, 024016 (2007), arXiv:0704.2667 [gr-qc].

[9] P. Bueno, P. A. Cano, F. Goelen, T. Hertog, and B. Vercnocke, Phys. Rev. D **97**, 024040 (2018), arXiv:1711.00391 [gr-qc].

[10] H. Yang, Z.-W. Xia, and Y.-G. Miao, Eur. Phys. J. C **85**, 742 (2025), arXiv:2406.00377 [gr-qc].

[11] S. Xin, B. Chen, R. K. L. Lo, L. Sun, W.-B. Han, X. Zhong, M. Srivastava, S. Ma, Q. Wang, and Y. Chen, Phys. Rev. D **104**, 104005 (2021), arXiv:2105.12313 [gr-qc].

[12] V. Cardoso, S. Hopper, C. F. B. Macedo, C. Palenzuela, and P. Pani, Phys. Rev. D **94**, 084031 (2016), arXiv:1608.08637 [gr-qc].

[13] V. Cardoso, E. Franzin, and P. Pani, Phys. Rev. Lett. **116**, 171101 (2016), [Erratum: Phys. Rev. Lett. 117, 089902 (2016)], arXiv:1602.07309 [gr-qc].

[14] Z. Mark, A. Zimmerman, S. M. Du, and Y. Chen, Phys. Rev. D **96**, 084002 (2017), arXiv:1706.06155 [gr-qc].

[15] A. Zimmerman, R. N. George, and Y. Chen, (2023), arXiv:2306.11166 [gr-qc].

[16] J. Abedi, H. Dykaar, and N. Afshordi, Phys. Rev. D **96**, 082004 (2017), arXiv:1612.00266 [gr-qc].

[17] J. Westerweck, A. Nielsen, O. Fischer-Birnholtz, M. Cabero, C. Capano, T. Dent, B. Krishnan, G. Meadors, and A. H. Nitz, Phys. Rev. D **97**, 124037 (2018), arXiv:1712.09966 [gr-qc].

[18] A. B. Nielsen, C. D. Capano, O. Birnholtz, and J. Westerweck, Phys. Rev. D **99**, 104012 (2019), arXiv:1811.04904 [gr-qc].

[19] M. R. Correia and V. Cardoso, Phys. Rev. D **97**, 084030 (2018), arXiv:1802.07735 [gr-qc].

[20] N. Uchikata, H. Nakano, T. Narikawa, N. Sago, H. Tagoshi, and T. Tanaka, Phys. Rev. D **100**, 062006 (2019), arXiv:1906.00838 [gr-qc].

[21] Q. Wang and N. Afshordi, Phys. Rev. D **97**, 124044 (2018), arXiv:1803.02845 [gr-qc].

[22] R. S. Conklin, B. Holdom, and J. Ren, Phys. Rev. D **98**, 044021 (2018), arXiv:1712.06517 [gr-qc].

[23] J. Ren and D. Wu, Phys. Rev. D **104**, 124023 (2021), arXiv:2108.01820 [gr-qc].

[24] A. Miani, C. Lazzaro, G. A. Prodi, S. Tiwari, M. Drago, E. Milotti, and G. Vedovato, Phys. Rev. D **108**, 064018 (2023), arXiv:2302.12158 [gr-qc].

[25] K. W. Tsang, M. Rollier, A. Ghosh, A. Samajdar, M. Agathos, K. Chatzioannou, V. Cardoso, G. Khanna, and C. Van Den Broeck, Phys. Rev. D **98**, 024023 (2018), arXiv:1804.04877 [gr-qc].

[26] R. Abbott *et al.* (LIGO Scientific, KAGRA, VIRGO), Astrophys. J. **966**, 137 (2024), arXiv:2210.10931 [astro-ph.HE].

[27] N. Uchikata, T. Narikawa, H. Nakano, N. Sago, H. Tagoshi, and T. Tanaka, Phys. Rev. D **108**, 104040 (2023), arXiv:2309.01894 [gr-qc].

[28] E. Maggio, A. Testa, S. Bhagwat, and P. Pani, Phys. Rev. D **100**, 064056 (2019), arXiv:1907.03091 [gr-qc].

[29] E. Maggio, *Probing new physics on the horizon of black holes with gravitational waves*, Ph.D. thesis, Rome U. (2022), arXiv:2211.16900 [gr-qc].

[30] E. Berti, V. Cardoso, M. H.-Y. Cheung, F. Di Filippo, F. Duque, P. Martens, and S. Mukohyama, Phys. Rev. D **106**, 084011 (2022), arXiv:2205.08547 [gr-qc].

[31] V. Cardoso, S. Biswas, and S. Sarkar (2025) arXiv:2511.14841 [gr-qc].

[32] N. Oshita, Q. Wang, and N. Afshordi, JCAP **04**, 016 (2020), arXiv:1905.00464 [hep-th].

[33] R. S. Conklin and N. Afshordi, (2021), arXiv:2201.00027 [gr-qc].

[34] J. L. Jaramillo, R. Panosso Macedo, and L. Al Sheikh, Phys. Rev. X **11**, 031003 (2021), arXiv:2004.06434 [gr-qc].

[35] R. A. Konoplya and A. Zhidenko, EPL **138**, 49001 (2022), arXiv:2203.16635 [gr-qc].

[36] V. Vellucci, E. Franzin, and S. Liberati, Phys. Rev. D **107**, 044027 (2023), arXiv:2205.14170 [gr-qc].

[37] A. Iannicciari, A. J. Iovino, A. Kehagias, P. Pani, G. Perna, D. Perrone, and A. Riotto, Phys. Rev. Lett. **133**, 211401 (2024), arXiv:2407.20144 [gr-qc].

[38] R. F. Rosato, S. Biswas, S. Chakraborty, and P. Pani, Phys. Rev. D **111**, 084051 (2025), arXiv:2501.16433 [gr-qc].

[39] L.-B. Wu, L. Xie, Y.-S. Zhou, Z.-K. Guo, and R.-G. Cai, (2025), arXiv:2509.20947 [gr-qc].

[40] E. P. Wigner, Phys. Rev. **98**, 145 (1955).